Under-Water Superaerophobic Pine-Shaped Pt Nanoarray Electrode for Ultrahigh-Performance Hydrogen Evolution

Yingjie Li, Haichuan Zhang, Tianhao Xu, Zhiyi Lu, Xiaochao Wu, Pengbo Wan, Xiaoming Sun,* and Lei Jiang*

A pine-shaped Pt nanostructured electrode with under-water superaerophobicity for ultrahigh and steady hydrogen evolution reaction (HER) performance is successfully fabricated by a facile and easily scalable electrodeposition technique. Due to the lower bubble adhesive force (11.5 ± 1.2 μN), the higher bubble contact angle (161.3° ± 3.4°) in aqueous solution, and the smaller size of bubbles release for pine-shaped Pt nanostructured electrode, the incomparable under-water superaerophobicity for final repellence of bubbles from submerged surface with ease, is successfully achieved, compared to that for nanosphere electrode and for Pt flat electrode. With the merits of superior under-water superaerophobicity and excellent nanoarray morphology, pine-shaped Pt nanostructured electrode with the ultrahigh electrocatalytic HER performance, excellent durability, no obvious current fluctuation, and dramatically fast current density increase at overpotential range (3.85 mA mV^{-1}, 2.55 and 13.75 times higher than that for nanosphere electrode and for Pt flat electrode, respectively), is obtained, much superior to Pt nanosphere and flat electrodes. The successful introduction of under-water superaerophobicity to in-time repel as-formed H_2 bubbles may open up a new pathway for designing more efficient electrocatalysts with potentially practical utilization in the near future.

1. Introduction

Hydrogen, as a clean fuel, is now being vigorously pursued as an alternative potential power source for traditional fossil fuels in the future. The electrocatalytic hydrogen evolution reaction (HER) is considered as one of the most efficient pathways to produce hydrogen.[1] Enormous electrocatalysts have thus been made to reduce the overpotential and consequently increase the efficiency of this important electrochemical process for pursuing sustainable and efficient hydrogen evolution.[2] The most effective electrocatalysts for HER up to now are noble metal Pt and its composites.[3] However, even for superior electrocatalysts, there exists a phenomenon that the as-formed gas bubbles stick to the traditional flat electrode surface, which hinder the contact of electrodes and electrolyte, increase Ohmic drop, and consequently result in the decrease of HER electrolysis efficiency.[4] Thus, developing effective HER electrocatalysts to efficiently disengage as-formed gas bubbles from electrode to improve the performance of HER electrocatalysts with low cost and high abundance still remains urgent.

Recently, lots of progress in obtaining low adhesion under-water superoleophobic surfaces by fabricating hierarchically micro/nanostructured interfaces[5] provide new opportunities to repel as-formed gas bubbles from electrode. Drawing an analogy to water drops on superhydrophobic surfaces, the gas bubbles are repelled from the submerged surfaces along with bubbles freely moving around surfaces in water, thus these surfaces are considered to be superaerophobic. As reported by Jiang and coworkers[6] in the air/water/solid system, the steadiness of three-phase contact line (TPCL) is crucial for the interactions between air bubbles and solid surface, while the hierarchically micro/nanostructures are effective for tailoring the air bubble pinning state.[6,7] Thus, the morphology of the electrocatalyst surface turns to be an important factor to affect the equilibrium state of gas bubble formation/detachment rapidly.[8] Very recently, we have demonstrated that the as-formed H_2 bubbles on under-water superaerophobic MoS_2 nanostructured electrodes could be easily driven off, yielding much higher current density increase under the given overpotential, attributing to their superaerophobic electrode surface with extremely low adhesive force to the surface.[9] However, the crystallinity of MoS_2 electrodes are of largely limited use in practice due to the relatively high solubility, poor electrochemical stability in the acid electrolyte, intrinsic bad electroconductivity, the preparation complexity, and poor scalability.[10] Furthermore, larger overpotential for nanostructured MoS_2 electrodes prevents their practical utilization compared with Pt and its composites possessing large cathodic current density with nearly zero overpotential.[2a] Meanwhile, the current density of the Pt flat and its composites electrode fluctuated obviously, suggesting that the electrode surface was working unstably when bubbles leaved the surface.

Y. Li, H. Zhang, T. Xu, Z. Lu, X. Wu, Dr. P. Wan, Prof. X. Sun
State Key Laboratory of Chemical Resource Engineering
Beijing University of Chemical Technology
P.O. Box 98, Beijing 100029, P.R. China
E-mail: pbwan@mail.buct.edu.cn;
sunxm@mail.buct.edu.cn

Prof. L. Jiang
Beijing National Laboratory for Molecular Sciences (BNLMS)
Institute of Chemistry, Chinese Academy of Sciences
Beijing 100190, P.R. China

DOI: 10.1002/adfm.201404250

Therefore, developing nanostructured Pt electrocatalysts with superaerophobicity and low adhesion force for gas evolution, facile preparation procedure and steady electrocatalytic performance, is an efficient way to simultaneously achieve high HER performance and long-term stability.

Herein, we fabricated a pine-shaped Pt nanostructured electrode with under-water superaerophobicity for ultrahigh and steady HER performance by a facile and easily scalable electrodeposition technique. The lower bubble adhesive force (11.5 ± 1.2 μN), the higher bubble contact angle (161.3° ± 3.4°) in aqueous solution, and the lower size of bubbles release for pine-shaped Pt nanostructured electrode, were successfully achieved, compared to that for nanosphere electrode and for Pt flat electrode, demonstrating the incomparable under-water superaerophobicity for final repellence of bubbles from submerged surface with ease. With the merits of superior under-water superaerophobicity and excellent nanoarray morphology, pine-shaped Pt nanostructured electrode with the ultrahigh electrocatalytic HER performance, excellent durability, no obvious current fluctuation, and dramatically fast current density increase at overpotential range (3.85 mA mV^{-1}, 2.55 and 13.75 times higher than that for nanosphere electrode and for Pt flat electrode, respectively), was obtained, in comparison with Pt nanosphere and flat electrodes.

2. Results and Discussion

Typically, as graphically depicted in **Figure 1**, Pt nanoarray and nanosphere electrodes were fabricated by variable electrodeposition method on inert Ti foil, which is a fast, simple, and cost-effective method and results in three-dimensional nanostructures directly grown on conductive substrates.[11] The nanostructures (i.e., nanoarray and nanosphere electrode) were well controlled by adjusting the rate of crystal growth and mass transport of growth units.[8,12] As demonstrated in **Figure 2**A and Figure S1, Supporting Information, the Pt nanoarray film was composed of pine-like units with very sharp edges, which greatly increased surface roughness, while the Pt nanosphere film consisted of relatively smooth nanosized Pt spheres with moderately increased roughness (Figure 2C and Figure S2, Supporting Information). The morphological differences between Pt nanoarray and nanosphere are striking. It is well known that the primary driving force for crystal growth is surface energy reduction,[13] and morphological formation of Pt nanoarray was attributed to reduction in surface energy adsorbed by hydrogen species (H_2 or H_{ads}), while anisotropic crystal growth rates of nanosphere led to spherical structures. In the control experiment, the Pt flat electrode with the lowest surface roughness was prepared by sputtering a continuous and dense Pt layer on Ti substrate (Figure 2E).

Inspired from the adhesive strength of the oil droplet on the film surface depended mainly on the wetting state/contact mode between the oil droplet and the film,[5a,14] the bubble adhesion behavior was mainly determined by the wetting state/contact mode on the under-water surface. Therefore, the wettability and bubble adhesion properties of the pine-shaped Pt nanoarray electrode, nanosphere electrode, and flat electrode were investigated. The bubble contact angle (CA) in aqueous solution and the corresponding contact angle hysteresis on Pt nanoarray film were 161.3° ± 3.4° (the inset of Figure 2B) and 2.8° (**Table 1**), respectively, displaying the superaerophobicity of Pt nanoarray film. This superaerophobicity was attributed to the intrinsically superaerophobic nanoarray structures with micro/nanoporous architecture, which cut the continuous TPCL of as-formed bubbles on electrode surface into a discrete state, made gas bubbles only touch the edges of the nanoarray and thus effectively reduced the contact area between the gas bubbles and the solid electrode (Figure S3A, Supporting Information). Therefore, an extremely low adhesive force to the

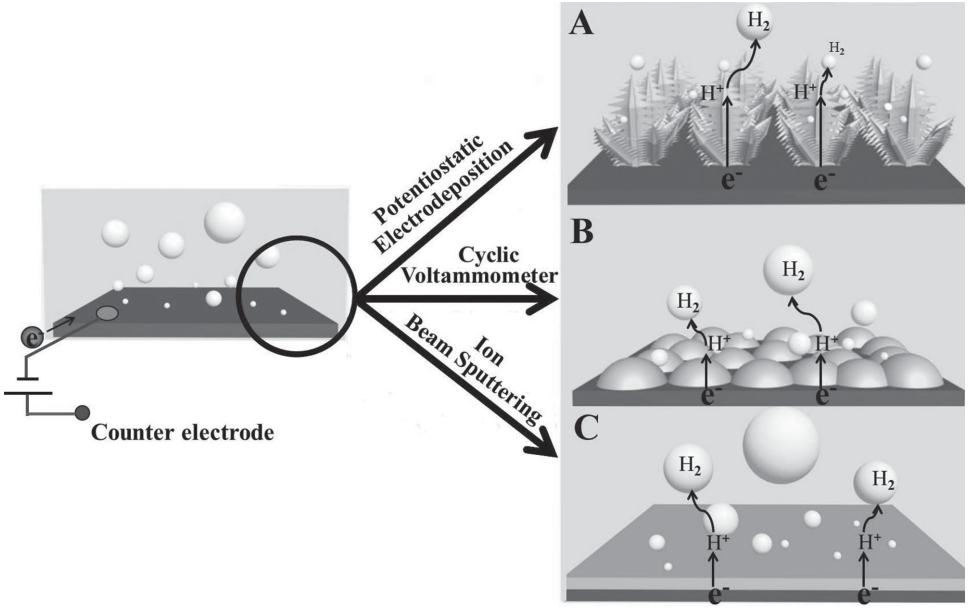

Figure 1. Schematic illustration of the preparation of various Pt electrodes: A) nanoarray, B) nanosphere, C) flat films on Ti foil and the corresponding electrocatalytic HER on different film surfaces with variable sizes of released bubbles.

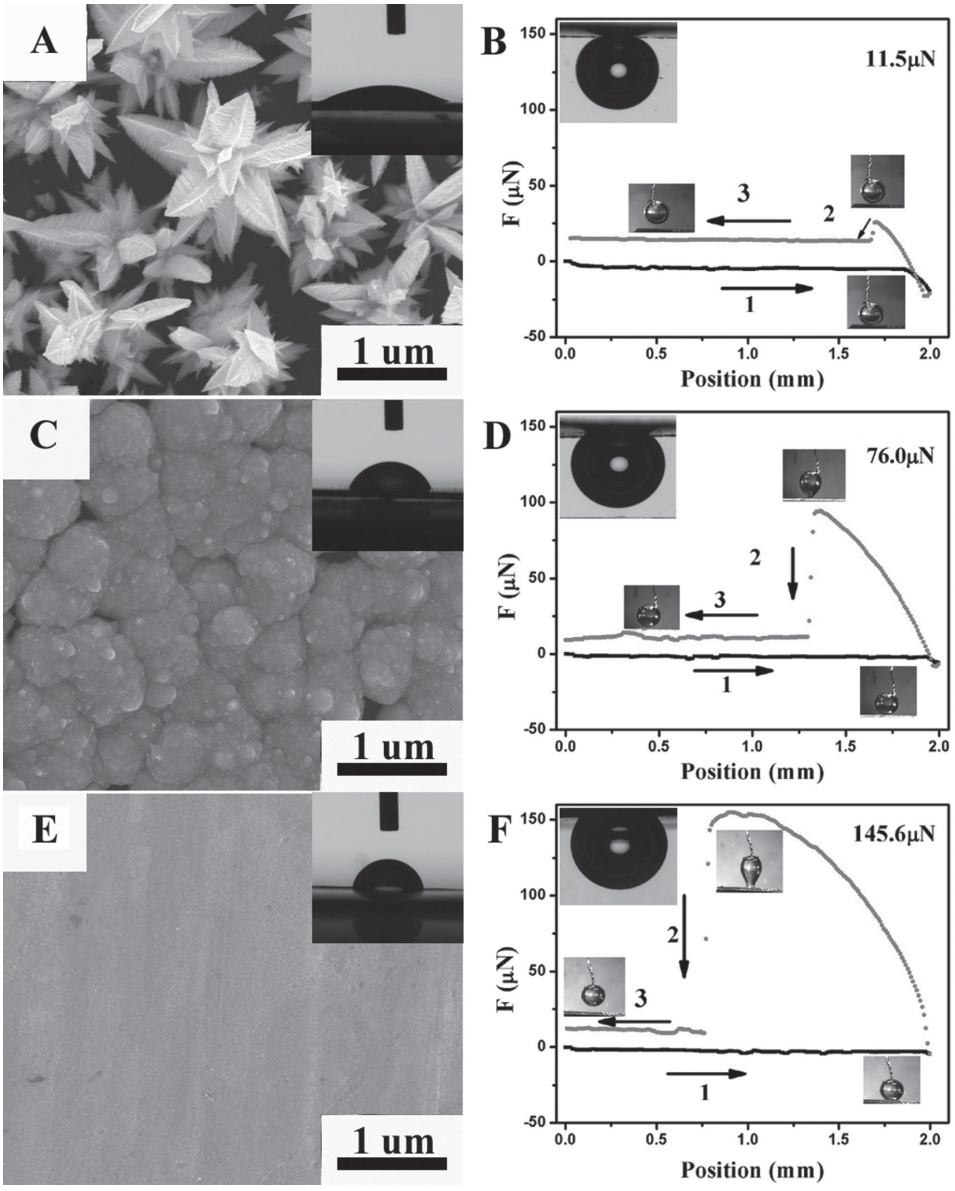

Figure 2. A) SEM image and B) gas bubble adhesive force measurement of Pt nanoarray film. The nanoarray architecture offers an extremely low bubble adhesive force (11.5 ± 1.2 μN). C) SEM image and D) gas bubble adhesive force measurement of Pt nanosphere film, showing a larger bubble adhesive force (76.0 ± 1.5 μN). E) SEM image and F) gas bubble adhesive force measurement of Pt flat film, where the largest bubble adhesive force is observed (145.6 ± 2.1 μN). As displayed in the insets for (A,C,E), the wetting ability test of Pt nanoarray film (the CA was measured as 29.3° ± 2.5°), Pt nanosphere film (64.9° ± 1.5°), and Pt flat film (81.4° ± 2.4°) to electrolyte (0.5 M H_2SO_4). In the insets of (B,D,F), the bubble CAs are 161.3° ± 3.4° for Pt nanoarray film, 144.2° ± 2.3° for Pt nanosphere film, and 129.4° ± 2.6° for Pt flat film. For gas bubble adhesive force measurement in (B,D,F), Process 1: the film surface approached to the air bubble; Process 2: the film surface left the air bubble; Process 3: the film surface broke away from the air bubble.

surface (11.5 ± 1.2 μN, Figure 2B) was observed for the Pt nanoarray structures with superaerophobicity, which was further confirmed by the negligible shape change of the bubble during gas bubble adhesive force measurement (Figure 2B). And consequently gas bubbles could be released from the surface with ease. In the experiment, the under-water gas adhesion was dynamically measured by a high-sensitivity microelectromechanical balance system, and a gas bubble was contacted with electrode surface then allowed to leave. Meanwhile, due to the good hydrophilicity of the Pt nanoarray electrode with the water CA of 29.3° ± 2.5° (the inset of Figure 2A), water could be easily trapped into micro/nanoporous architecture of the Pt nanoarray electrode surface to form a wetting film. Therefore, when H_2 gas bubbles were generated on the electrode under solution, the water would wet into the hydrophilic micro/nanoporous architecture to form "water reservoirs" and the "water reservoirs" reduced the contact area for the gas bubbles on the solid electrode and consequently lowered the bubbles adhesive force, which benefited the rapid bubble formation and the bubble release.

In the control experiment, the Pt nanosphere electrode (Figure 2C and Figure S2, Supporting Information) was

Table 1. Electrolyte and bubble CAs, advancing angles, receding angles, and hysteresis for Pt nanoarray, Pt nanosphere, and Pt flat electrodes.

Samples	CA of gas bubbles [°]	Advancing angle [°]	Receding angle [°]	Hysteresis [°]
Pt nanoarray	161.3	162.2	159.4	2.8
Pt nanosphere	144.4	148.6	141.1	7.5
Pt flat	136.7	141.4	126.0	15.4

constructed with packed nanospheres, which moderately decreased the roughness. As reported that the increase in roughness led to a continuous change of contact mode of the gas on the films, and a change in wetting behavior from Wenzel, Wenzel–Cassie transition, to the Cassie regime.[5a] Therefore, it is obvious that the decrease of roughness could increase the contact area for the gas bubbles on the solid electrode (Figure S3B, Supporting Information) compared with that for Pt nanoarray electrode, resulting in the increased adhesive force to bubbles (76.0 ± 1.5 μN, Figure 2D). However, the value was still much lower than that for Pt flat electrode (145.6 ± 2.1 μN, Figure 2F). The gas bubble was attached to the flat electrode surface, which possessed the highest contact area with the gas bubbles attached to the flat surface to form a continuous and stable TPCL (Figure S3C, Supporting Information). The continuous TPCL generated high gas adhesion and CA hysteresis (Table 1), resulting in the difficulty for the gas bubbles detached away from electrode surface. Therefore, smaller under-water gas bubble CAs (144.2° ± 2.3° and 129.4° ± 2.6°) and larger CA hysteresis (7.5° and 15.4°) were obtained for Pt nanosphere electrode and Pt flat electrode (Figure 2D,F and Table 1). Meanwhile, the water CAs of Pt nanosphere electrode and Pt flat electrode were 64.9° ± 1.5°and 81.4° ± 2.4° (inset in Figure 2C,E), demonstrating their weaker hydrophilicity than that for Pt nanoarray electrode. These results clearly demonstrated the importance of the specific architecture of nanoarray electrode surface with variable wetting state, contact mode and surface roughness for reducing the gas bubble contact area and gas bubble adhesion force to form superaerophobicity, which are desirable for efficient bubble release during HER.

The bubble releasing behaviors during electrocatalytic HER were recorded by employing an optical microscope lens with a charge-coupled device (CCD) camera system to get enough bubble images for further analysis. All the images were taken at the same hydrogen production speed (60 mA cm^{-2}) for comparison. The generated bubbles removed away from the Pt nanoarray electrode surface (**Figure 3**A) so quickly before they grew larger than ≈150 μm in diameter and the major sizes of bubbles were largely distributed at <50 μm (Movie S1, Supporting Information, for the gas evolution video). This fast release of H_2 bubbles decreased the unavailable active sites for HER. As for the Pt nanosphere electrode, the junctions between nanospheres cut the continuous integrated solid film into discrete surface which in some degree impeded the bubble evolution behavior with the released bubble sizes at 150–250 μm in diameter (Figure 3B and Movie S2, Supporting Information). For the Pt flat film, similar fraction of the film surface with the Pt nanoarray and nanosphere films could generate H_2 bubbles as seen in Movie S3, Supporting Information. However, the as-formed bubbles adhered to the surface strongly and could hardly be detached until the bubbles were large up to ≈500 μm (Figure 3C and Movie S3, Supporting Information). Although some bubbles with the size less than ≈300 μm in diameter existed, only larger bubbles (>450 μm in diameter) were released from the film surface and the smaller bubbles continued to grow up at the same time. Above results demonstrated that the superaerophobic Pt nanoarray electrode could benefit in quick removal of small H_2 bubbles from the electrode surface, which should be critical for improving the HER performance of electrodes, and thus achieving a faster HER current increasing.

Gas evolution from electrode surface usually brings disturbance to electrode and electrolyte solution, which are reflected in the electrochemical curves.[15] For three types of electrodes, the corresponding bubble incubation and release behaviors were recorded as time-dependent current curve with different serrate shapes (**Figure 4**A), attributing to different current turbulence caused by the growth and release of various sizes of bubbles attached to the surface of electrodes, the lager bubbles size and more obvious fluctuation. In comparison to the nanoarray and nanosphere electrode, the flat electrode exhibited the largest current fluctuation with a totally typical serrate shape. The "serrate" herein indicated the asymmetric fluctuation of currents. Always, the current decreased slowly, indicating the slow growth of bubbles. Then the current increased sharply, corresponding to the detachment of bubbles from the electrode surface when they grew beyond the critical sizes. The digital images in inset of Figure 4A showed hydrogen evolution process with bubbles "emergence", "growth" (accumulation), and "release" states on Pt flat electrode and their corresponding current changes, respectively. Obviously, the Pt nanosphere and flat electrodes with gradually enhanced adhesion behaviors to the bubbles exhibited relatively lager sizes of released H_2 bubbles, while Pt nanoarray electrode could effectively promote the releasing process of H_2 bubbles, providing a steady working condition.

The electrocatalytic HER activities of our three different types of electrodes were performed in 0.5 M H_2SO_4 solution continuously purged with H_2 (g) and were corrected for IR losses under the similar system resistance (1.6 ± 0.1 Ω, Figure S4, Supporting Information). Polarization curves showed the geometric current density against the applied potential for representative samples of the different Pt electrode morphologies, as shown in Figure 4B. The comparison in Figure 4B showed that the Pt electrode morphology played an irreplaceable role in the electrocatalysis performance. Clearly, the cathodic current rose rapidly under more negative potential for the Pt nanoarray electrode, compared with that for Pt nanosphere and flat electrodes. Specially, the Pt nanoarray electrode exhibited the fastest cathodic current density increase of ≈3.85 mA mV^{-1}, which was 2.55 times higher than that of Pt nanosphere and 13.75 times more than that of Pt flat electrode when electrochemical surface areas (ECSA) of Pt nanoarray electrode was twice as much as that of Pt flat electrode (Figure S5 and Table S1, Supporting

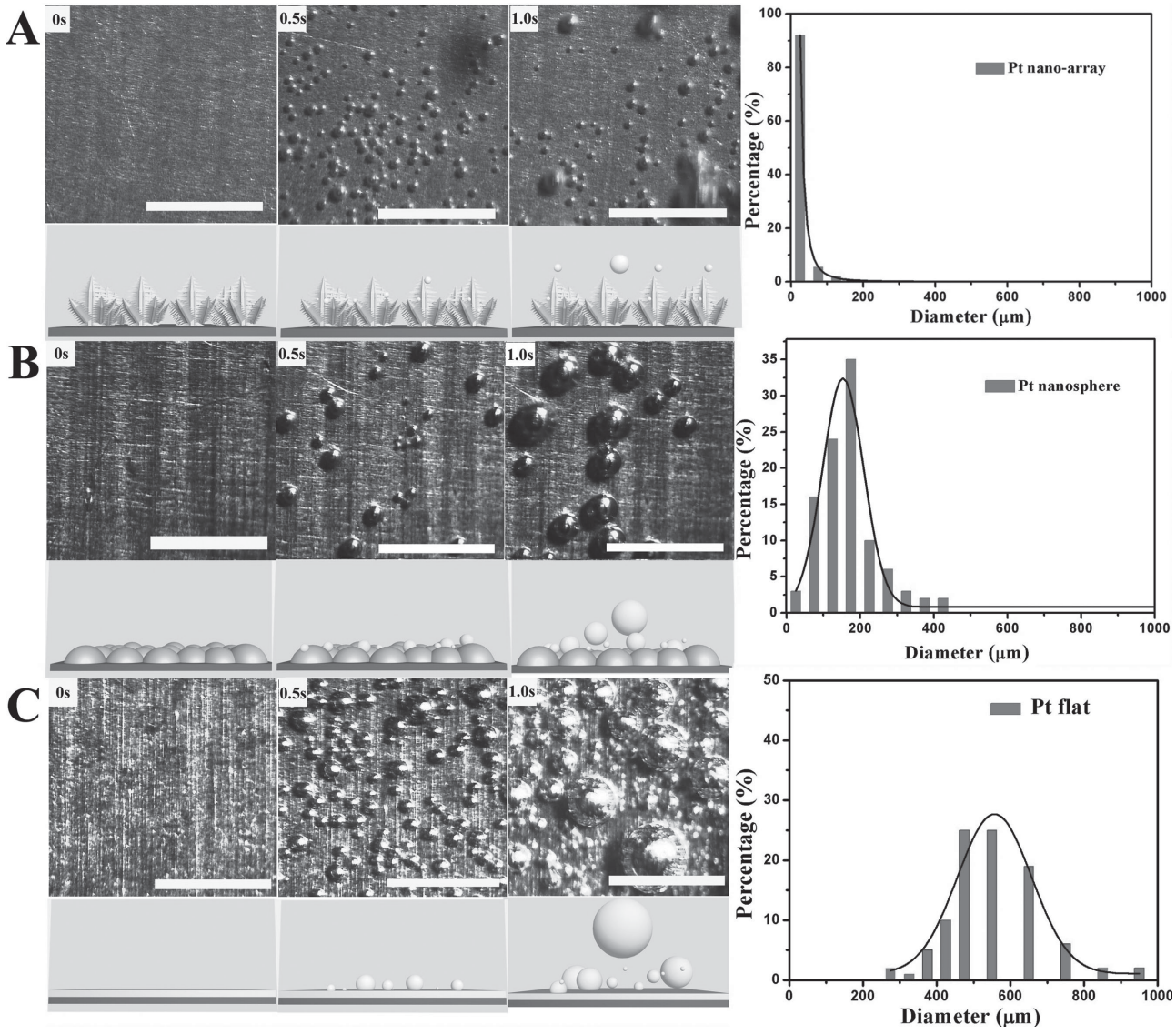

Figure 3. Digital images showing different bubble generation behaviors and the corresponding statistics of the related size distribution for the released bubbles on A) Pt nanoarray film, B) Pt nanosphere film, and C) Pt flat film. Scale bar: 500 μm.

Information).[16] The excellent electrocatalytic HER performance of Pt nanoarray electrode with no obvious fluctuation was probably related to the low adhesion behaviors to the bubbles, and consequently easy removal of as-formed bubbles with small sizes from the Pt nanoarray electrode surface, exposing the larger contact area of electrodes with electrolyte and more active sites for HER. From Figure S6, Supporting Information, due to some porous structrures inside the nanosphere which greatly increased ECSA, a close ECSA was detected for Pt nanosphere electrode (21.77 m^2 g^{-1}, Figure 4C and Table S1, Supporting Information) compared to that for Pt nanoarray electrode (22.32 m^2 g^{-1}). However, slower HER current density increase was observed for Pt nanosphere electrode (Figure 4B), ascribing to the unavailability of the effective sites for HER, and release of the bubbles in larger sizes.

Long-term stability for HER was assessed in evaluating electrochemical catalysts. Over the duration of a 36 h stability measurement, the current density of the Pt nanoarray electrode at constant potential (–0.5 V vs SCE) was very stable (Figure 4D, black line), while the corresponding current density for Pt flat electrode rapidly reduced, with a large drop occurring within 0.4 h (Figure 4D, red line), likely caused by the physical loss of electrocatalyst material as we show later. The Pt nanosphere electrode showed improved stability relative to flat electrode during condition of continuous hydrogen evolution, however, it eventually also suffered from the physical loss of Pt material, as indicated by the decrease of ≈20 mA cm^{-2} at the applied potential of –0.55 V versus SCE (Figure 4D, blue line).

The stability difference was relative to the structure difference as revealed by surface morphology characterization (**Figure 5** and Figure S7, Supporting Information). SEM images of Pt nanoarray and nanosphere electrodes after the working stability test (Figure 5A,B) were also obtained to assess possible morphological changes as a result of electrocatalytic HER. Only

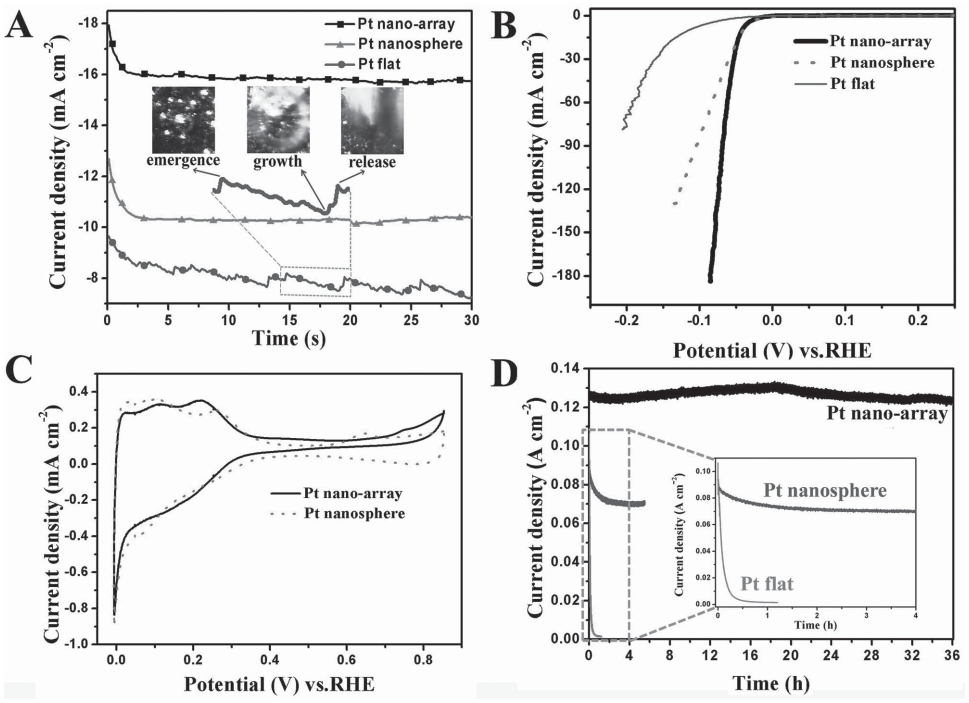

Figure 4. A) *i–t* curves for Pt nanoarray electrode, Pt nanosphere electrode, and Pt flat electrode. The obvious current fluctuation of flat electrode indicates the slow growth of bubbles and rapid detachment from the electrode surface. The inset of digital images of the inset reveals bubbles emergence, accumulation, and release, respectively. B) Polarization curves obtained for Pt nanoarray electrode, Pt nanosphere electrode, and Pt flat electrode. The onset potential of Pt nanoarray electrode is near 0 mV and the current density increases rapidly. C) CV curves obtained for the Pt nanoarray electrode and Pt nanosphere electrode in N_2-saturated 0.5 M H_2SO_4 solutions at 10 mV s^{-1}. D) Long-term stability measurements for representative Pt nanoarray, Pt nanosphere, and Pt flat electrodes, illustrating the greatly enhanced stability of the Pt nanoarray electrode compared to the nanosphere and flat electrodes.

a trace of morphology changes of the Pt nanoarray sharp edges could be detected (Figure 5A and Figure S7B, Supporting Information), and little morphology changes and loss of some nanospheres were obtained for Pt nanosphere electrode (Figure 5B and Figure S7D, Supporting Information), while dramatic damage was observed for Pt flat electrode after continuous bubbles evolution in Figure 5C: after continuous HER, the flat thin Pt nanosphere had shrunken into several isolated nanoparticles, and some of these nanoparticles got lost and left behind some caves on the substrates (Figure 5C and Figure S7F, Supporting Information). This could be understood from the point view of bubble size and adhesion force difference. The flat electrode adhered bubbles 10 times larger of size than the nanoarray electrodes, which meant 1000 times of detachment force difference (proportional to volume). So much stronger interactions of the bubbles with electrodes would make the bubbles scratch/drag the surficial electrochemical active materials from the electrode and cause loss of them and thus fade them. While for the nanoarray electrode, the electrode could be kept stable by significantly reducing the bubble scratch/drag force to less than 1/1000. In general, the nanoarray electrode without obvious morphology changes possessed more working stability and higher HER activity than that for Pt nanosphere and flat electrodes, ascribing to the low adhesion behaviors to the bubbles, and easy removal of as-formed bubbles with small sizes and no obvious fluctuation during rapid H_2 bubbles evolution. Compared with commercial Pt/C film, the Pt nanoarray electrode also exhibited incomparable electrocatalytic activity and good stability (Figure S8, Supporting Information). These results clearly

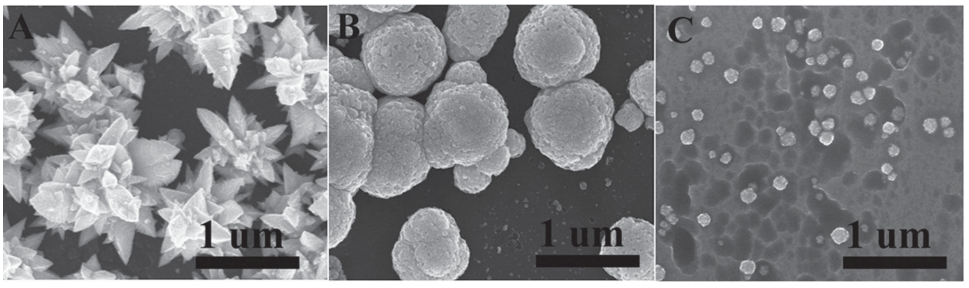

Figure 5. SEM images of measured A) Pt nanoarray, B) nanosphere, and C) flat electrodes after stability test. In the case of nanosphere and flat electrodes, rapid H_2 (g) evolution can damage the electrode, while nanoarray electrode are relatively stable.

illustrated that the bubble adhesive force and superhydrophilicity played an important role in the electrocatalytic HER performance.

3. Conclusion

In summary, the pine-shaped Pt nanostructured electrode with the lower gas bubble contact area, the lower gas bubble adhesion force and the lower size of released bubbles to form under-water superaerophobicity for ultrahigh (≈3.85 mA mV^{-1}, 13.75 times higher than Pt flat electrode) and steady HER performance (≈100% retention after 36 h working) was successfully achieved by facile electrodeposition technique, compared with that for nanosphere electrode and for Pt flat electrode. The success of introducing micro/nanoporous architecture into nanoarray electrode surface with variable wetting state, contact mode and surface roughness for reducing the gas bubble contact area and gas bubble adhesion force to form superhydrophilicity, which are desirable for efficient bubble release and thus efficiently electrocatalytic HER performance. We believe that this line of research can be applicable for other gas evolution materials to improve the electrocatalytic activity and pave a new way for designing more efficient gas evolution electrocatalysis.

4. Experimental Section

$H_2PtCl_6{\cdot}6H_2O$ and KNO_3 were obtained from Sinopharm Chemical Reagent Co., Ltd. Other materials, such as H_2SO_4 (≈98 wt%), HCl (≈38 wt%), and CH_3CH_2OH (≈99.7 wt%) were all of A.R. grade, purchased from Beijing Chemical Reagent Co., Ltd, and used as received.

Pt nanoarray film and Pt nanosphere film were electroplated on Ti substrates (1 cm × 1 cm) and the experimental setup for the preparation of Pt nanoarray and Pt nanosphere films were described elsewhere.[17] The working electrode was a Ti plate while carbon paper was used as counter electrode and a saturated calomel electrode (SCE) was used as reference electrode. The Pt nanoarray was prepared by potentiostatic electrodeposition with the deposition potential up to –0.3 V, while Pt nanosphere film was electroplated via cyclic electrodeposition with potential controlled in a range from –0.2 to 0.5 V at scan rate 0.01 V s^{-1} for 15 cycles. H_2PtCl_6 (3×10^{-3} M) solution with KNO_3 (100×10^{-3} M) was employed as supporting electrolyte in both of the electrodeposition processes. The electrodeposition solution was kept at a temperature of 30 °C. Before the electrodeposition, the Ti substrates were first mechanically polished, and then sonicated in concentrated HCl solution (≈37 wt%), and cleaned with de-ionized water and absolute ethanol for 5 min, respectively. Finally the Ti substrates were thoroughly rinsed with de-ionized water and dried at 80 °C for 0.5 h.

The size and morphology of the samples were characterized using a field-emission SEM (Zeiss SUPRA 55) operating at 20 kV and a High-resolution TEM system (Titan) operating at 200 kV. We characterized the wettability of the film surface by measuring the CAs of 0.5 M H_2SO_4 (electrolyte). In these experiments, 2.5 µL of the electrolyte was dropped on the film surface, and the CA was measured on Dataphysics OCA20 system (optical CA measurement) in ambient air at room temperature.

The electrochemical measurements were carried out at room temperature in a three-electrode glass cell connected to an electrochemical workstation (CHI 660D, Chenghua, Shanghai). Prior to the test measurements, hydrogen was bubbled through the electrolyte solution to eliminate the dissolved oxygen and to maintain a fixed Nernst potential for the H^+/H_2 redox couple. Linear sweep voltammetry with scan rate of 1 mV s^{-1} was conducted in 0.5 M H_2SO_4 solution using saturated calomel electrode as the reference electrode. Carbon paper was used as the counter electrode. AC impedance measurements were carried out in the same configuration at potential of –0.3 V (vs SCE) from 10^5–0.1 Hz with an AC voltage of 5 mV. In all measurements, we used saturated calomel electrode as the reference. It was calibrated with respect to reversible hydrogen electrode (RHE) by using Pt electrode as standard electrode (SCE 0.262 vs RHE). The bubble incubation and release behaviors were detected under –0.05, –0.05, and –0.1 V (potential vs RHE) for nanoarray, nanosphere, and flat electrode, respectively. The stability test of the electrodes were operated under a series of potentials (–0.5, –0.55, and –0.6 V vs SCE) for nanoarray, nanosphere, and flat electrode at similar system resistance (1.6 ± 0.1 Ω) for achieving a high initial current density.

A high-speed charge-coupled device camera (i-SPEED, OLYMPUS) was mounted on a microscope (SZ-CTC, OLYMPUS) for continuous imaging of hydrogen bubble releasing process. The illumination was achieved by a fiber optic illuminator system (Multi-Position, Nikon).

The bubble CA was measured by the captive bubble method (Dataphysics OCA20) and was defined as the observed equilibrium CA of liquid around the pinned bubbles on a solid surface, where the liquid/gas interface meets the solid/liquid interface across the three phase contact interfaces. The volume of the gas bubble was about 3 µL for each testing. The advancing angle and receding angle were measured by the increasing and then decreasing a certain volume (ca. 2 µL) of gas bubbles. All experiments have been repeated for >5 times.

The interaction force between the gas bubbles and electrode interfaces can be assessed by a high-sensitivity micro-electromechanical balance system (Dataphysics DCAT21, Germany). An optical microscope lens and a charge-coupled device camera system were used to take photographs at the rate of one frame per second. The electrode surface was placed in a square quartz cell (50 mm × 50 mm × 50 mm) filled with 0.5 M H_2SO_4 (electrolyte), and the cell was fixed to the plate of the balance system. Gas bubble (≈2 µL) was suspended on a metal ring in the 0.5 M H_2SO_4, and the force of this balance system was initially set to zero. The electrodes were moved upward at a constant speed of 0.01 mm s^{-1} until their surfaces contacted the air bubble. The force was increased gradually until it reached its maximum and the shape of the air bubble changed from spherical to elliptical. Subsequently, when the electrode moved down further, the contact was sharply reduced to near zero and the shape of the air bubble changed back to spherical.

Supporting Information

Supporting Information is available from the Wiley Online Library or from the author.

Acknowledgements

This work was financially supported by National Natural Science Foundation of China, the 973 Program (Grant Nos. 2011CBA00503 and 2011CB932403), the Fundamental Research Funds for the Central Universities, Beijing Natural Science Foundation (2152023).

Received: December 1, 2014
Revised: January 13, 2015
Published online: February 10, 2015

[1] H. Wang, Z. Lu, S. Xu, D. Kong, J. J. Cha, G. Zheng, P. C. Hsu, K. Yan, D. Bradshaw, F. B. Prinz, Y. Cui, *Proc. Natl. Acad. Sci.* **2013**, *110*, 19701.

[2] a) Y. Li, H. Wang, L. Xie, Y. Liang, G. Hong, H. Dai, *J. Am. Chem. Soc.* **2011**, *133*, 7296; b) Y. Sun, C. Liu, D. C. Grauer, J. Yano, J. R. Long, P. Yang, C. J. Chang, *J. Am. Chem. Soc.* **2013**, *135*, 17699; c) N. Danilovic, R. Subbaraman, D. Strmcnik, K. C. Chang, A. P. Paulikas, V. R. Stamenkovic, N. M. Markovic, *Angew. Chem. Int. Ed.* **2012**, *51*, 12495; d) C. G. Morales-Guio, S. D. Tilley, H. Vrubel, M. Gratzel, X. Hu, *Nat. Commun.* **2014**, *5*, 3059;

e) Y. Wang, G. Zhang, W. Xu, P. Wan, Z. Lu, Y. Li, X. Sun, *ChemElectroChem* **2014**, *1*, 1138.
[3] a) Y. Liu, D. Gokcen, U. Bertocci, T. P. Moffat, *Science* **2012**, *338*, 1327; b) X. Huang, Z. Zeng, S. Bao, M. Wang, X. Qi, Z. Fan, H. Zhang, *Nat. Commun.* **2013**, *4*, 1444; c) H. Zhang, Y. Li, G. Zhang, P. Wan, T. Xu, X. Wu, X. Sun, *Electrochim. Acta* **2014**, *148*, 170; d) Y. Ding, M. W. Chen, J. Erlebacher, *J. Am. Chem. Soc.* **2003**, *126*, 6876.
[4] a) S. K. Mazloomi, N. Sulaiman, *Renew. Sust. Energ. Rev.* **2012**, *16*, 4257; b) M. S. Faber, R. Dziedzic, M. A. Lukowski, N. S. Kaiser, Q. Ding, S. Jin, *J. Am. Chem. Soc.* **2014**, *136*, 10053.
[5] a) Y. Huang, M. Liu, J. Wang, J. Zhou, L. Wang, Y. Song, L. Jiang, *Adv. Funct. Mater.* **2011**, *21*, 4436; b) X. Chen, Y. Wu, B. Su, J. Wang, Y. Song, L. Jiang, *Adv. Mater.* **2012**, *24*, 5884.
[6] J. Wang, Q. Yang, M. Wang, C. Wang, L. Jiang, *Soft Matter* **2012**, *8*, 2261.
[7] a) J. Wang, Y. Zheng, F. Q. Nie, J. Zhai, L. Jiang, *Langmuir* **2009**, *25*, 14129; b) D. Wu, S. Z. Wu, Q. D. Chen, Y. L. Zhang, J. Yao, X. Yao, L. G. Niu, J. N. Wang, L. Jiang, H. B. Sun, *Adv. Mater.* **2011**, *23*, 545; c) J. Wu, J. Xia, W. Lei, B. P. Wang, *Sci. Rep.* **2013**, *3*, 3268.
[8] S. H. Ahn, S. J. Hwang, S. J. Yoo, I. Choi, H.-J. Kim, J. H. Jang, S. W. Nam, T.-H. Lim, T. Lim, S.-K. Kim, J. J. Kim, *J. Mater. Chem.* **2012**, *22*, 15153.
[9] Z. Lu, W. Zhu, X. Yu, H. Zhang, Y. Li, X. Sun, X. Wang, H. Wang, J. Wang, J. Luo, X. Lei, L. Jiang, *Adv. Mater.* **2014**, *26*, 2683.
[10] J. Xie, H. Zhang, S. Li, R. Wang, X. Sun, M. Zhou, J. Zhou, X. W. Lou, Y. Xie, *Adv. Mater.* **2013**, *25*, 5807.
[11] a)X. Xu, X. Zhang, H. Sun, Y. Yang, X. Dai, J. Gao, X. Li, P. Zhang, H. H. Wang, N. F. Yu, S. G. Sun, *Angew. Chem. Int. Ed.* **2014**, *126*, 12730; b) L. X. Ding, A. L. Wang, G. R. Li, Z. Q. Liu, W. X. Zhao, C. Y. Su, Y. X. Tong, *J. Am. Chem. Soc.* **2012**, *134*, 5730.
[12] L.-L. Li, C.-W. Chang, H.-H. Wu, J.-W. Shiu, P.-T. Wu, E. Wei-Guang Diau, *J. Mater. Chem.* **2012**, *22*, 6267.
[13] J. Wang, L. Wei, L. Zhang, Y. Zhang, C. Jiang, *Cryst. Eng. Commun.* **2012**, *14*, 1629.
[14] a) L. Chen, G. Yang, S. Wang, *Small* **2012**, *8*, 962; b) S. Wang, L. Jiang, *Adv. Mater.* **2007**, *19*, 3423.
[15] a) M. J. Kenney, M. Gong, Y. Li, J. Z. Wu, J. Feng, M. Lanza, H. Dai, *Science* **2013**, *342*, 836; b) J. Yang, K. Walczak, E. Anzenberg, F. M. Toma, G. Yuan, J. Beeman, A. Schwartzberg, Y. Lin, M. Hettick, A. Javey, J. W. Ager, J. Yano, H. Frei, I. D. Sharp, *J. Am. Chem. Soc.* **2014**, *136*, 6191.
[16] a) X. Liu, D. Wang, Y. Li, *Nano Today* **2012**, *7*, 448; b) F. Saleem, Z. Zhang, B. Xu, X. Xu, P. He, X. Wang, *J. Am. Chem. Soc.* **2013**, *135*, 18304.
[17] A. Ponrouch, S. Garbarino, E. Bertin, C. Andrei, G. A. Botton, D. Guay, *Adv. Funct. Mater.* **2012**, *22*, 4172.